ISSN: 1999-6691, e-ISSN: 2782-3709 DOI: 10.7242/1999-6691/2026.19.1.3

Research article

The onset and evolution of nonlinear convective regimes of binary mixtures in multilayer systems simulating synclinal geological folds

I.S. Shubenkov, T.P. Lyubimova

Institute of Continuous Media Mechanics UB RAS, Perm, Russian Federation

This paper studies three-dimensional convective regimes of a binary mixture in a system of three porous bent layers, simulating a synclinal geological fold under the influence of a geothermal temperature gradient. The layers are assumed to have identical porosities and different permeabilities. A mixture of tetralin and dodecane taken in equal proportions is considered as the fluid saturating the porous medium. The components of the mixture represent the groups of hydrocarbons found in oil fields. The numerical study is performed to evaluate the linear stability of the mechanical equilibrium of a binary mixture in the inclined porous layer saturated with liquid in a gravity field under the influence of a strictly vertical temperature gradient. The convection threshold found is compared with the threshold obtained for the system with non-linear stability. In three-dimensional nonlinear calculations for a three-layer mixture, the permeabilities of all three layers are varied. Here it is assumed that the permeabilities of the outer layers are identical and always lower than the permeability of the inner layer. It was found that when the permeability of the inner layer is much higher than the permeabilities of the outer layers, the flow is localized in the inner layer. When the permeabilities of the outer and inner layers are sufficiently close, the flow is localized near the outer boundaries of the fold, even if the inner layer is more permeable than the outer layers. As the supercriticality increases, the formation of longitudinal rolls is observed in the initially plane-parallel flow (within each fold limb), and the flow becomes spiral. A further increase in supercriticality leads to a predominance of the longitudinal roll component in the flow and an increase in the number of longitudinal rolls along the fold limb (increase in the wave number of longitudinal rolls).

Keywords: thermal convection, binary mixture, porous media, multilayer system, inclined layer, vertical temperature gradient, mathematical modeling, ANSYS Fluent

Received: 04.11.2025 / *Published online*: 04.04.2026

1. Introduction

Geological structures are layered rock formations that differ in porosity and permeability. When rock strata undergo plastic deformation, they are folded. A fold is called anticlinal (anticline) if the layers are bent convex upward (older strata occur in the core, younger strata in the limbs) and synclinal if it is convex downward [1, 2].

Such fluid-saturated layered systems become natural subsurface reservoirs for naturally occurring convective processes [3–6]. One of the commonly used approaches to modeling heterogeneous porous media is to consider a system of layers with different porosity and permeability values, while assuming these properties to be homogeneous within each individual layer [7–12].

Solving such problems requires topographic and geological data and is often performed either neglecting thermal convection or assuming a single-component fluid [8, 10, 13, 14]. However, fluids and gases saturating porous media generally have a complex composition. This necessitates accounting for diffusion, thermodiffusion, and related effects [15–17].

Thermal convection in inclined porous layers saturated with fluids is usually studied in cases where the layer boundaries are maintained at different constant temperatures and mechanical equilibrium is impossible. For arbitrarily small temperature differences, a steady flow always exists; once the temperature gradient reaches a certain value, this flow loses stability and a secondary flow arises in addition to the basic one.

In [18, 19], the onset and development of thermal convection in an inclined fluid-saturated porous layer in a gravitational field under a strictly vertical temperature gradient were investigated. It was established that, for any angle of

©Authors 2026 Translation of the original article in Russian This is an open access article under the CC BY 4.0 license

inclination, longitudinal rolls (convective rolls with axes directed along the layer and perpendicular to the axis with respect to which the layer is inclined) are the most dangerous type of perturbation. For inclination angles $\alpha < 45^\circ$, the critical perturbations are long-wave, whereas for $\alpha > 45^\circ$ they are cellular. Two-dimensional perturbations (rolls with axes parallel to the axis with respect to which the layer is inclined) are also possible in the system, but they are not the most dangerous.

In [20], the Soret effect was taken into account in the study of three-dimensional convection of a binary mixture in a three-layer porous system simulating an anticlinal geological fold under a vertical geothermal temperature gradient. The porosities of the layers were assumed equal, whereas their permeabilities were different. Within the framework of linear stability analysis, it was found that for any layer inclination angle the most dangerous mode is represented by cellular longitudinal rolls. Nonlinear calculations showed that, at low permeabilities of all layers, the resulting flow is long-wave in character. As the permeability of the middle layer increases, the flow in the plane of the geological fold limbs takes the form of cellular longitudinal rolls, in agreement with the results of linear stability analysis. The flow is localized in the middle layer and substantially affects the impurity concentration field.

The present paper continues and extends the study of a system of porous layers simulating an anticlinal fold [20]. Here, a synclinal fold is considered, and unlike [20], where the permeabilities of the outer layers were assumed to be below the threshold value and, consequently, convective motion did not penetrate into these layers, a wider range of permeability ratios is considered, including nearly equal permeabilities, when convection becomes possible in all three layers.

2. Problem formulation

We consider Soret-induced convection of a binary mixture of tetralin (50%) and dodecane (50%) in a porous medium. These substances are typical representatives of hydrocarbons contained in crude oil. The viscosity and transport coefficients are assumed constant. Barodiffusion and diffusion-thermal conductivity are neglected. The lighter component, tetralin, is treated as the impurity, whereas the heavier component, dodecane, is regarded as the solvent. The mixture density ρ is assumed to depend linearly on temperature T and impurity concentration C:

$$\rho = \rho_0(1 - \beta_T(T - T_0) - \beta_C(C - C_0)). \tag{1}$$

Here, $\beta_T = -\dfrac{1}{\rho_0}\dfrac{\partial \rho}{\partial T}\bigg|_C$ is the thermal expansion coefficient; $\beta_C = -\dfrac{1}{\rho_0}\dfrac{\partial \rho}{\partial C}\bigg|_T$ is the solutal expansion coefficient; ρ_0 and T_0, C_0 are, respectively, the mean values of the mixture density and temperature, and the impurity concentration.

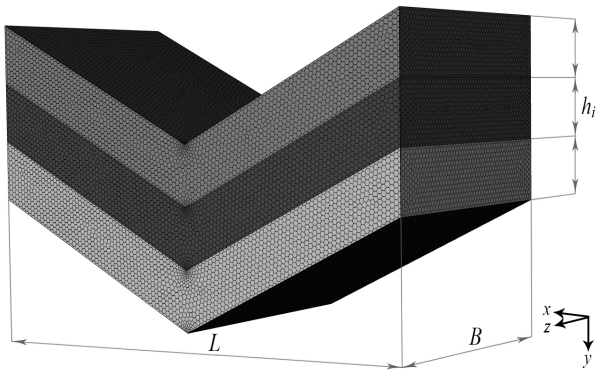


Fig. 1. Model of a synclinal fold

The mixture fills a cavity representing a system of three layers of equal thickness $h_i = 25$ m, with a bend in the central part, thus simulating a synclinal geological fold (Fig. 1). The length of the computational domain is $L = 200$ m, and the width is $B = 100$ m. Such dimensions are typical of hydrocarbon-bearing strata. For these geometric dimensions, the fold angle (the angle between the inclined planes) is approximately 152°. The geometry and boundary conditions are analogous to those used in [20].

The modeling is performed within the Darcy–Boussinesq framework [15], taking thermodiffusion into account:

$$0 = -\frac{1}{\rho_0}\nabla P_i - \frac{\nu}{K_i}\mathbf{V}_i - \mathbf{g}(\beta_T(T_i - T_0) + \beta_C(C_i - C_0)), \tag{2}$$

$$(\rho c)^* \frac{\partial T_i}{\partial t} + (\rho c)_f \mathbf{V}_i \cdot \nabla T_i = \lambda^* \nabla^2 T_i, \tag{3}$$

$$\varepsilon^* \frac{\partial C_i}{\partial t} + \mathbf{V}_i \cdot \nabla C_i = D^* \nabla^2 C_i + C_0(1 - C_0) D_T^* \nabla^2 T_i, \tag{4}$$

$$\nabla \cdot \mathbf{V}_i = 0. \tag{5}$$

Here, $\mathbf{V}$ is the filtration velocity vector; P is the pressure; $\mathbf{g}$ is the gravitational acceleration vector; t is time; K_i is the permeability of the ith layer; ν is the kinematic viscosity of the mixture; λ^* and $(\rho c)^*$ are the effective thermal conductivity and heat capacity of the porous medium; $(\rho c)_f$ and ε^* are the heat capacity and porosity of the mixture; $D^* = D/\tau^2$ and $D_T^* = D_T/\tau^2$ are the coefficients of molecular diffusion and thermodiffusion of the mixture in the porous medium; τ is the tortuosity factor of the porous medium [21, 22]. The index $i = 1,2,3$ denotes the layer number (from top to bottom).

Bottom heating with a temperature gradient of $A = 3 \cdot 10^{-2}$ K/m is considered (which corresponds to the average geothermal gradient [23]). The value used in the calculations, $T_0 = 353.5$ K, is the mean temperature at an oil occurrence depth of $2 \cdot 10^3$ m under the average geothermal gradient.

On the boundaries Γ of the computational domain, the following conditions are imposed:
– no-flow and zero diffusive mass flux conditions are prescribed on all external boundaries;
– on the upper and lower faces (indices T and B), the temperature corresponds to a strictly vertical geothermal gradient;
– on the vertical faces, the heat flux is zero;
– on the interfaces between the layers (indices 1 and 2), the pressure, temperature, and concentration, as well as the normal components of the heat and diffusive mass fluxes and the normal projections of the velocity vector, are continuous:

$$x = 0; L: \quad \mathbf{V}_i \cdot \mathbf{n} = 0, \quad \frac{\partial T_i}{\partial n} = 0, \quad \frac{\partial C_i}{\partial n} = 0, \tag{6}$$

$$z = 0; B: \quad \mathbf{V_i} \cdot \mathbf{n} = 0, \quad \frac{\partial T_i}{\partial n} = 0, \quad \frac{\partial C_i}{\partial n} = 0, \tag{7}$$

$$y = y_{\Gamma_T}: \quad \mathbf{V}_1 \cdot \mathbf{n} = 0, \quad T_1 = T_0 + Ay, \quad \frac{\partial (C_1 - \Theta T_1)}{\partial n} = 0, \tag{8}$$

$$y = y_{\Gamma_B}: \quad \mathbf{V}_3 \cdot \mathbf{n} = 0, \quad T_3 = T_0 + Ay, \quad \frac{\partial (C_3 - \Theta T_3)}{\partial n} = 0, \tag{9}$$

$$y = y_{\Gamma_1}: \quad P_1 = P_2, \quad \mathbf{V}_1 \cdot \mathbf{n} = \mathbf{V}_2 \cdot \mathbf{n}, \quad \frac{\partial T_1}{\partial n} = \frac{\partial T_2}{\partial n}, \quad T_1 = T_2, \quad \frac{\partial (C_1 - \Theta T_1)}{\partial n} = \frac{\partial (C_2 - \Theta T_2)}{\partial n}, \quad C_1 = C_2, \tag{10}$$

$$y = y_{\Gamma_2}: \quad P_2 = P_3, \quad \mathbf{V}_2 \cdot \mathbf{n} = \mathbf{V}_3 \cdot \mathbf{n}, \quad \frac{\partial T_2}{\partial n} = \frac{\partial T_3}{\partial n}, \quad T_2 = T_3, \quad \frac{\partial (C_2 - \Theta T_2)}{\partial n} = \frac{\partial (C_3 - \Theta T_3)}{\partial n}, \quad C_2 = C_3. \tag{11}$$

Here, $\mathbf{n}$ is the unit normal vector, $\Theta = \psi(\beta_T/\beta_C)$, where $\psi = C_0(C_0 - 1)\beta_C D_T/(\beta_T D)$.

It is assumed that initially the fluid is at rest, the impurity concentration is uniform throughout the cavity, and the temperature depends linearly on the vertical coordinate.

3. Parameters and numerical implementation

The physical properties of the tetralin (50%)–dodecane (50%) mixture are listed in the table. It is important to note that studies of heat and mass transfer in porous media [21, 22] have revealed the need to correct the effective diffusion and thermodiffusion coefficients. Accordingly, the values $D^* = 2.81 \cdot 10^{-10}$ m^2/s and $D_T^* = 2.6 \cdot 10^{-12}$ m^2/(sK) were used in the simulations. These values correspond to the following dimensionless parameters: the separation ratio $\psi = 0.694$, and the Lewis number $\mathrm{Le} = \chi/D = 150$, where χ is the thermal diffusivity.

Table. Physical and thermal parameters of the tetralin (50%)–dodecane (50%) mixture

ρ_0, kg/m^2	ν, m^2/s	χ, m^2/s	β_T, 1/K	β_C	D, m^2/s	D_T, m^2/(sK)
840.70	$1.81 \cdot 10^{-6}$	$9.70 \cdot 10^{-8}$	$8.95 \cdot 10^{-4}$	0.270	$6.46 \cdot 10^{-10}$	$5.94 \cdot 10^{-12}$

The porosity values were taken equal to 0.1 for all layers. The permeabilities of the upper and lower layers were assumed equal and always smaller than the permeability of the inner layer. The calculations were performed for layer permeabilities in the range from $2 \cdot 10^{-11}$ to 10^{-14} m^2. Such medium properties are typical, for example, of fine-grained sand, clayey sands, siltstones, microfractured limestones, sandstone, and shales [24–27].

The computations were carried out using the ANSYS Fluent software package implementing the finite volume method. A spatial mesh with poly-hexahedral cells and edge sizes ranging from 0.5 to 2.0 m was employed. Spatial discretization was performed using the second-order MUSCL (Monotone Upstream-Centered Schemes for Conservation Laws) scheme. At each time step, the convergence criterion for the velocity components was that the absolute residuals should be less than 10^{-3} (and less than 10^{-6} for the energy equation). The simulations were run up to times of the order of 10^4-10^5 years with a time step of 10^7 s (0.317 years).

Under a strictly vertical geothermal temperature gradient, the system under consideration may admit a state with no convective motion. To determine the stability conditions for this state, a simplified problem was solved, namely, the linear stability of the no-convection state in an infinite inclined porous layer saturated with a binary fluid with the Soret effect taken into account under a strictly vertical temperature gradient was investigated.

4. Linear problem: formulation and solution method

Consider an infinite horizontal layer of thickness $2h$ of porous medium saturated with a binary mixture and inclined at an angle α to the vertical (Fig. 2). The system is placed in a gravitational field. We assume that the upper and lower boundaries of the system are impermeable, rigid, and perfectly heat-conducting. At the system boundaries, we prescribe a temperature distribution corresponding to a strictly vertical temperature gradient.

Assume that the mixture density, according to Eq. (1), depends linearly on temperature and impurity concentration. The problem will be solved using the equations of free convection of a binary fluid in a porous medium with the Soret effect taken into account: (2)–(5).

To introduce dimensionless variables (with subscript *ND*) for length, velocity, time, pressure, temperature, and concentration, we use the following scales: $y=h\cdot y_{ND}$, $V=\dfrac{a}{h}\cdot V_{ND}$, $t=\dfrac{h^2(\rho c)^*}{\lambda^*}\cdot t_{ND}$, $P=\dfrac{\rho_0 av}{K}\cdot P_{ND}$, $T=Ah\cdot T_{ND}$, $C=C_0(C_0-1)AhD_T(D)^{-1}\cdot C_{ND}$. Here, $a=\lambda^*/(\rho c)_f$ is the effective thermal diffusivity.

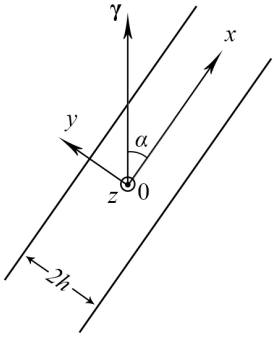


Fig. 2. Computational scheme of the linear problem

The system of equations (2)–(5) in dimensionless form becomes

$$0=-\nabla P-\mathbf{V}+\mathrm{Ra}(T+\psi C)\boldsymbol{\gamma}, \tag{12}$$

$$\frac{\partial T}{\partial t}+\mathbf{V}\cdot\nabla T=\nabla^2 T, \tag{13}$$

$$\varepsilon\frac{\partial C}{\partial t}+\mathbf{V}\cdot\nabla C=\mathrm{Le}^{-1}\left(\nabla^2 C-\nabla^2 T\right), \tag{14}$$

$$\nabla\cdot\mathbf{V}=0, \tag{15}$$

where $\mathrm{Ra}=\dfrac{Kg\beta_T h^2 A}{av}$ is the Rayleigh-number analogue for a porous medium (hereafter referred to simply as the "Rayleigh number"), ψ is the dimensionless separation ratio introduced above, A is the value of the vertical temperature gradient, $\varepsilon=\varepsilon^*\dfrac{(\rho c)_f}{(\rho c)^*}$ is the normalized porosity, and $\boldsymbol{\gamma}$ is the upward unit vector.

At the system boundaries, we impose the impermeability condition, prescribe a temperature distribution corresponding to a strictly vertical temperature gradient in the layer, and assume zero impurity flux. In dimensionless form, these conditions read

$$-1\leqslant y\leqslant 1: \qquad V_y=0, \qquad T=-A(x-x_0)\cos\alpha-A(y-y_0)\sin\alpha, \qquad \frac{\partial C}{\partial y}-\frac{\partial T}{\partial y}=0. \tag{16}$$

The problem under consideration admits a solution corresponding to the no-convection state:

$$\tilde{V}=0, \qquad \nabla\tilde{T}=-\boldsymbol{\gamma}, \qquad \nabla\tilde{C}=-\boldsymbol{\gamma}, \qquad \nabla\tilde{P}=\mathrm{Ra}(T_0+\psi C_0)\boldsymbol{\gamma}. \tag{17}$$

We now perform a linear stability analysis of state (17). To this end, all fields are represented as sums of the basic-state fields and a small perturbation:

$$V=\tilde{V}+V', \qquad T=\tilde{T}+T', \qquad C=\tilde{C}+C', \qquad P=\tilde{P}+P'. \tag{18}$$

Substituting these expressions into Eqs. (12)–(15) and linearizing with respect to the perturbations, we express the velocity field through its components in all equations and write the equation of motion (12) in projected form on the coordinate axes. Eliminating V_x, V_z, and P from the resulting equations, we introduce normal perturbations periodic in the x and z directions (written in complex form):

$$V'=\varphi(y)e^{i(k_x x+k_z z)},$$
$$T'=\theta(y)e^{i(k_x x+k_z z)},$$
$$C'=\xi(y)e^{i(k_x x+k_z z)},$$

k_x, k_z are the wave numbers in the x and z directions, respectively.

As a result, we arrive at a system of equations for the perturbation amplitudes of the velocity component — $\varphi(y)$, temperature — $\theta(y)$, and concentration — $\xi(y)$. For convenience, we introduce a new function: $\eta=\xi-\theta$, which is a combination of the concentration and temperature perturbations. Then the system of equations for the amplitudes φ,θ,η takes the form

$$\Delta\varphi+i\zeta k\,\mathrm{Ra}\cos\alpha\cdot[\theta'(\psi+1)+\psi\cdot\eta']+k^2\,\mathrm{Ra}\sin\alpha\cdot[\theta(\psi+1)+\psi\cdot\eta]=0, \tag{19}$$

$$\Delta\theta+\varphi\sin\alpha+i\frac{\zeta}{k}\varphi'\cos\alpha+\left(1-\zeta^2\right)\mathrm{Ra}\cos^2\alpha\,[\theta(\psi+1)+\psi\cdot\eta]=0, \tag{20}$$

$$\Delta\eta+\mathrm{Le}\,\varphi\sin\alpha+i\,\mathrm{Le}\,\frac{\zeta}{k}\varphi'\cos\alpha+\mathrm{Le}\left(1-\zeta^2\right)\mathrm{Ra}\cos^2\alpha\,[\theta(\psi+1)+\psi\cdot\eta]=0, \tag{21}$$

where $k^2=k_x^2+k_z^2$, $\Delta=\partial_{yy}^2-k^2$, $\zeta=k_x/k$ is the three-dimensionality parameter.

The boundary conditions for φ,θ,η are

$$y=\pm1:\ \ \varphi=0,\quad \theta=0,\quad \frac{\partial\eta}{\partial y}=0. \tag{22}$$

Next, the problem described by system (19)–(21) with boundary conditions (22) will be solved numerically. To this end, we construct a fundamental system of solutions consisting of six first-order differential equations, implemented using the fifth-order Runge–Kutta method. The zero of the determinant of the matrix of the fundamental system of solutions is found by the secant method. Detailed information on the solution procedure can be found in [28].

5. Estimation of the critical Rayleigh number

Unlike the conventional linear model, in which oil-bearing formations are represented by infinitely extended layers, the geometry considered in the present study is more complex. Therefore, the linear model is used only for a preliminary estimate of the critical Rayleigh number, while the main focus is placed on the investigation of the nonlinear dynamics of the system.

Let us estimate the critical Rayleigh number for the inner layer under the assumption that convection does not penetrate into the outer layers (for example, when their permeability is substantially lower). Calculations performed at the Lewis number $\mathrm{Le}=150$ and the separation ratio $\psi=0.694$, corresponding to the tetralin (50%)–dodecane (50%) mixture, yield the critical Rayleigh number $\mathrm{Ra}=0.0142$. The most dangerous perturbations are those at $\zeta=0$ (longitudinal rolls), whereas the least dangerous ones correspond to $\zeta=1$ (plane perturbations) (Fig. 3). This Rayleigh number corresponds to the permeability value at which convection in the outer layers becomes possible, namely, $K=6.02\cdot10^{-16}$ m^2. In the nonlinear study of the system, however, convection was found to start at a permeability of the order of $K\approx10^{-15}$ m^2.

6. Three-dimensional nonlinear calculations

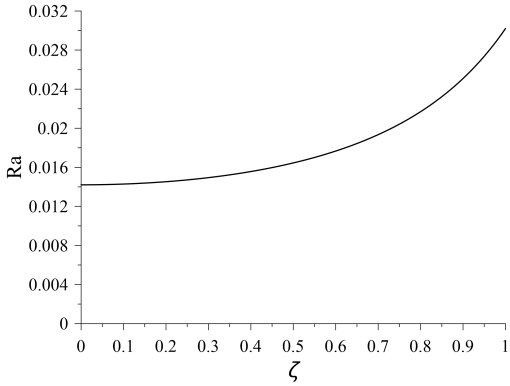


Fig. 3. Dependence of the critical Ra on ζ at $\alpha = 76^\circ$, $\psi = 0.694$

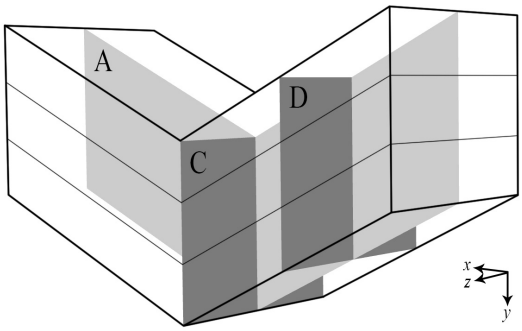


Fig. 4. Planes in which the results of the nonlinear calculations are presented

Below, the results of nonlinear calculations performed in the ANSYS Fluent software package are presented for a synclinal fold with different layer permeabilities. The permeabilities of the outer layers were taken equal. The dimensional parameters of the system corresponded to the tetralin (50%)–dodecane (50%) mixture (see the Table in Section 3). Figure 4 shows the planes in which the fields obtained in double precision using the nonlinear model for the unsteady problem formulation will be presented below. The planes are arranged as follows:

– A cuts the fold in half perpendicular to the z axis;
– C separates the left limb of the fold from the right one and is perpendicular to the x axis;
– D is located in the middle of the right limb and is perpendicular to the x axis.

Example 1. First, let us examine the flow in layers with low permeabilities and, accordingly, small supercriticalities (that is, near the convection threshold): $K_{in} = 10^{-13}$ m^2 in the inner layer and $K_{ex} = 10^{-14}$ m^2 in the outer layers. For this permeability ratio ($K_p = K_{in}/K_{ex} = 10$), a large-scale plane-parallel flow arises, concentrated predominantly in the central layer but also involving the less permeable outer layers (see Figs. 5–7). There is no fluid motion along the z axis. The flow noticeably distorts the impurity concentration isolines in plane A (Fig. 7).

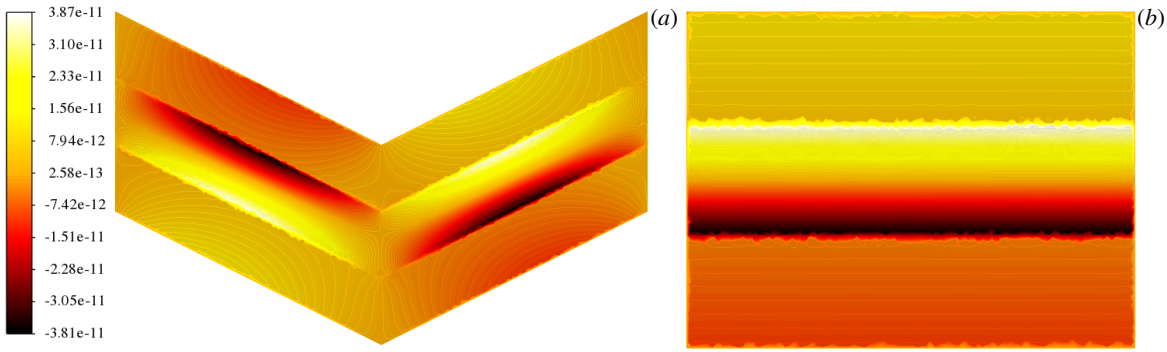


Fig. 5. Fields of the velocity component V_x [m/s] at $K_p = K_{in}/K_{ex} = 10$ in planes A (*a*) and D (*b*)

Example 2. Let us see how the system responds to a twofold decrease in the permeability of the inner layer, namely, $K_{in} = 5 \cdot 10^{-14}$ m^2, $K_{ex} = \cdot 10^{-14}$ m^2, $K_p = 5$. This makes the permeabilities of the outer and inner layers closer, but, as

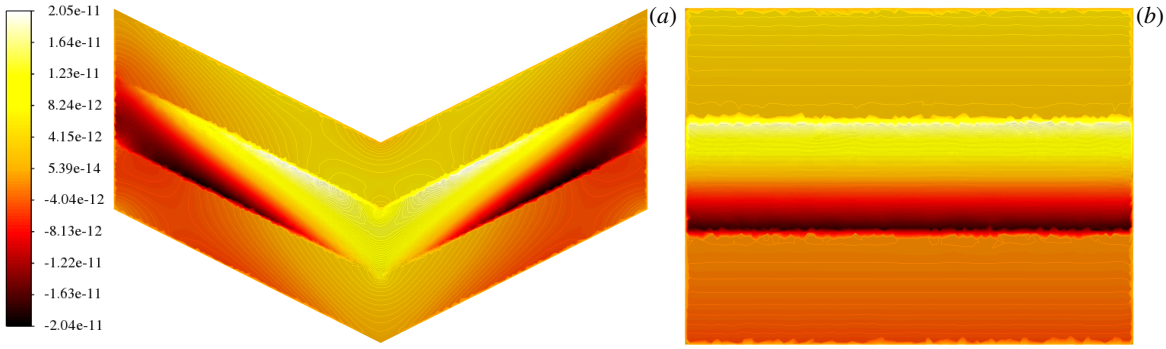


Fig. 6. Fields of the velocity component V_y [m/s] at $K_p = K_{in}/K_{ex} = 10$ in planes A (*a*) and D (*b*)

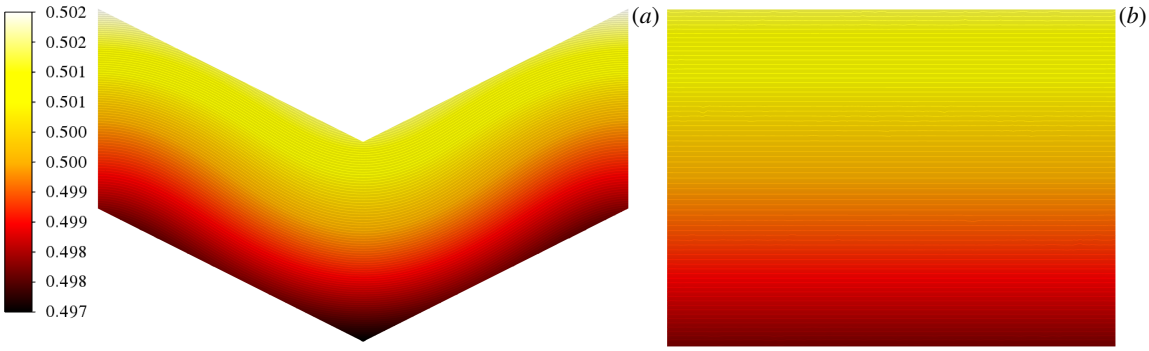


Fig. 7. Impurity concentration fields at $K_p = K_{in}/K_{ex} = 10$ in planes A (*a*) and D (*b*)

expected, leads to a decrease in the overall intensity of convection. Under these parameters, a flow qualitatively similar to that in Example 1 is observed; however, the fluid fluxes in the less permeable outer layers become more intense than those in the inner layer. Because of the overall decrease in flow intensity, the impurity concentration isolines are distorted to a lesser extent. In this case, the concentration distribution approaches its linear vertical gradient.

Example 3. Next, let us further reduce the permeability of the inner layer so that it becomes only twice as large as the permeability of the outer layers ($K_{in} = 2 \cdot 10^{-14}$ m^2, $K_{ex} = 10^{-14}$ m^2, $K_p = 2$). As can be seen from Figs. 8–10, the main fluid flow occurs in the outer layers, although they are less permeable than the inner one. This is because the flow within each fold limb becomes large-scale, unlike in Examples 1 and 2: one convective roll occupies all layers of the limb. At the same time, the flow is most intense near the upper and lower boundaries of the fold. However, on the whole, the flow intensity decreases again because of the reduced permeability of the inner layer. As a consequence, the impurity concentration isolines (Fig. 10) are distorted even less than in Example 2.

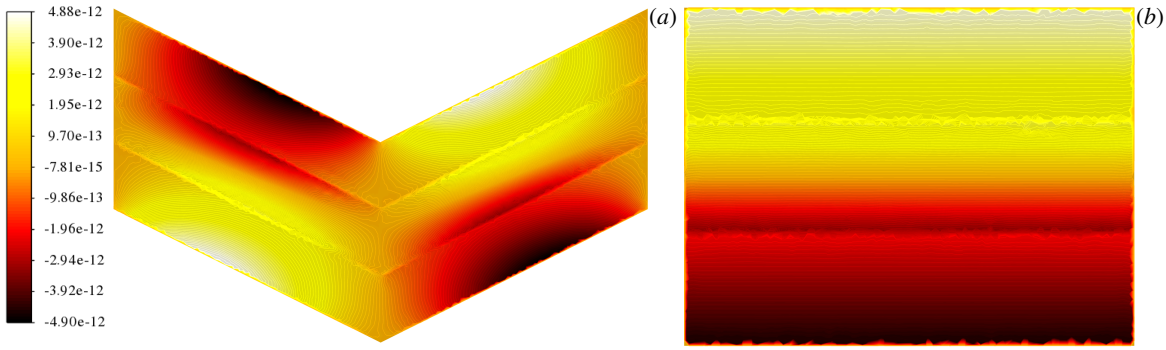


Fig. 8. Fields of the velocity component V_x [m/s] at $K_p = K_{in}/K_{ex} = 2$ in planes A (*a*) and D (*b*)

Example 4. Now let us examine the effect of increasing the permeability of all layers by one order of magnitude compared with Example 1: $K_{in} = 10^{-12}$ m^2, $K_{ex} = 10^{-13}$ m^2. In this case, $K_p = 10$ still holds and, as in Examples 1 and 2,

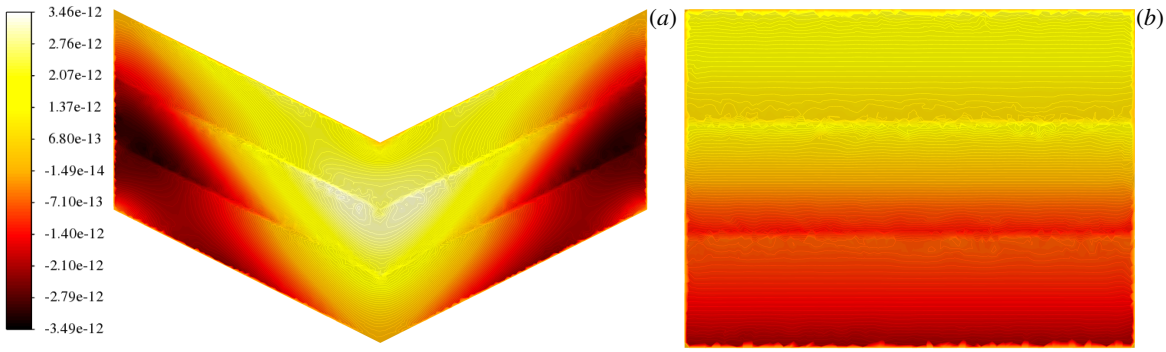


Fig. 9. Fields of the velocity component V_y [m/s] at $K_p = K_{in}/K_{ex} = 2$ in planes A (a) and D (b)

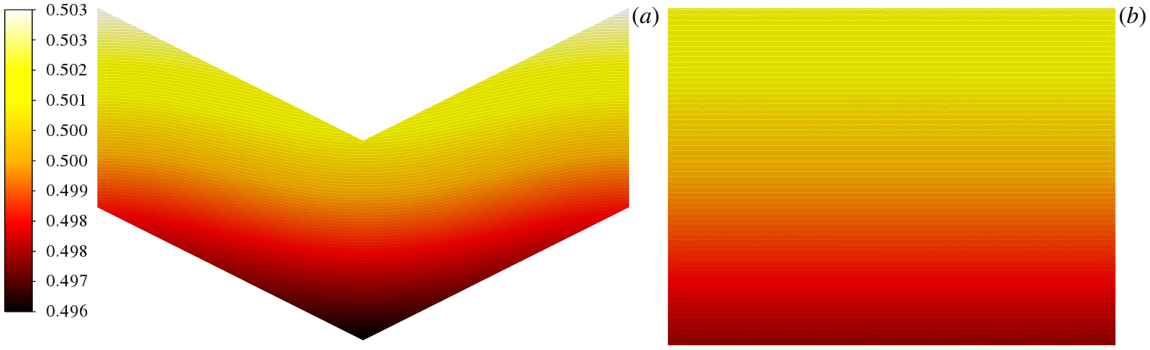


Fig. 10. Impurity concentration fields at $K_p = K_{in}/K_{ex} = 2$ in planes A (a) and D (b)

a large-scale plane-parallel flow is observed, concentrated predominantly in the central layer but also involving the less permeable outer layers. However, unlike the cases with lower layer permeabilities (Examples 1 and 2), the flow becomes more intense, and the peaks of its intensity along the y axis shift toward the center and the edges of the fold. For the system with smaller K_p (that is, with close permeabilities of all layers), behavior qualitatively similar to that already discussed in Examples 1–3 is observed. The only exception in Example 4 is that, owing to the increased flow intensity, the concentration field isolines are now distorted even more strongly (Fig. 11).

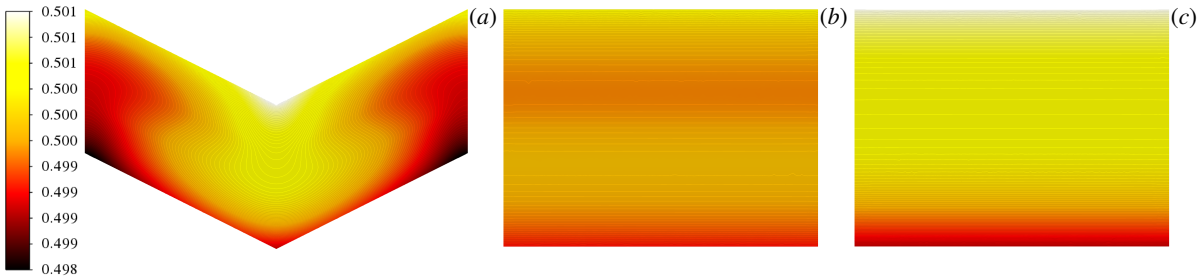


Fig. 11. Impurity concentration fields at $K_p = K_{in}/K_{ex} = 10$ in planes A (a), D (b), and C (c)

Example 5. Relative to Example 4, let us increase the permeability of the outer layers by one order of magnitude: $K_{ex} = 10^{-12}$ m^2, while taking the permeability of the inner layer to be five times larger than that of the outer layers: $K_{in} = 5 \cdot 10^{-12}$ m^2, that is, $K_p = 5$. As can be seen from Figs. 12–15, a large-scale plane-parallel flow with superposed longitudinal rolls is observed (a flow with a four-vortex structure). The fluid velocity along the z axis is now nonzero, that is, the flow becomes three-dimensional. The main fluid motion occurs in the outer layers, despite the fact that they are less permeable than the inner one. It is noteworthy that when all layers forming the fold are more permeable, redistribution of the regions of high flow intensity occurs in a similar way at higher values of K_p. The flow along the x axis is most intense near the upper and lower boundaries of the fold, whereas the flow along the y axis is most intense at the ends of the fold

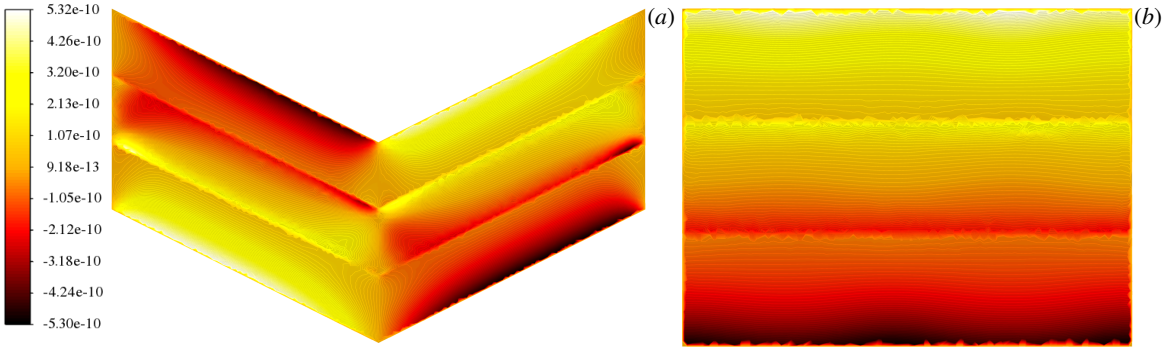


Fig. 12. Fields of the velocity component V_x [m/s] at $K_p = K_{in}/K_{ex} = 5$ in planes A (*a*) and D (*b*)

and in its center. Owing to the influence of the longitudinal rolls, the impurity concentration isolines become strongly curved (Fig. 16), both in plane A and in planes D and C.

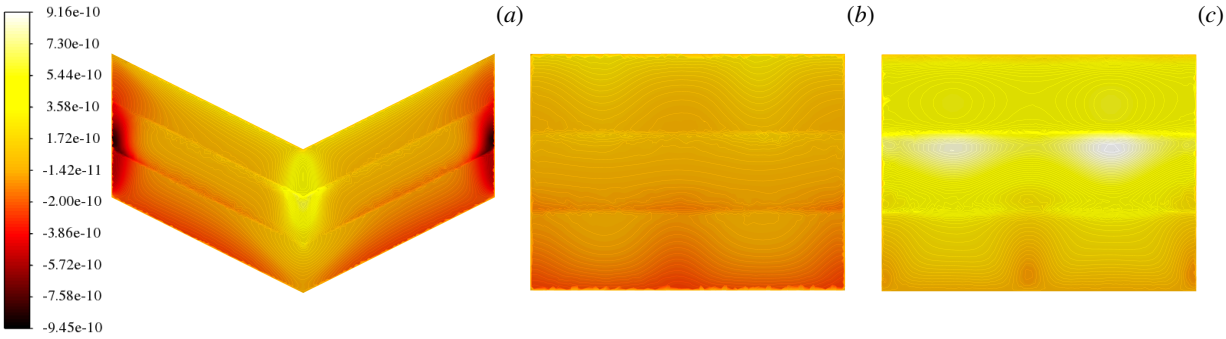


Fig. 13. Fields of the velocity component V_y [m/s] at $K_p = K_{in}/K_{ex} = 5$ in planes A (*a*) and D (*b*)

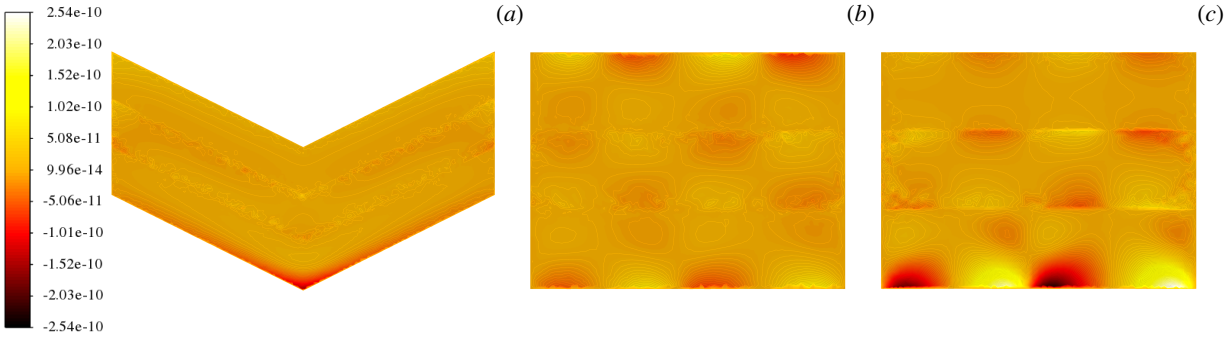


Fig. 14. Fields of the velocity component V_z [m/s] at $K_p = 5$ in planes A (*a*), D (*b*), and C (*c*)

Example 6. Let us increase the permeability of the inner layer tenfold and that of the outer layers fivefold compared with Example 5: $K_{in} = 5 \cdot 10^{-11}$ m^2, $K_{ex} = 5 \cdot 10^{-12}$ m^2, $K_p = 10$. In this case, the flow is large-scale with superposed longitudinal rolls (with a five-vortex structure) (Fig. 17), and the main contribution to the fluid motion comes from the longitudinal rolls. The flow is intense throughout the whole volume; however, zones of localization can be distinguished near the ends and around the center of the fold. The concentration field isolines (Fig. 18) are curved even more strongly than in Example 5. At the outer-layer permeability $K_{ex} = 5 \cdot 10^{-12}$ m^2 and smaller K_p (that is, for close permeabilities of all layers), the system behavior is qualitatively similar to the cases considered above.

Thus, the convection threshold obtained in the nonlinear calculations turns out to be close to the convection threshold revealed by the linear stability analysis performed in Section 5.

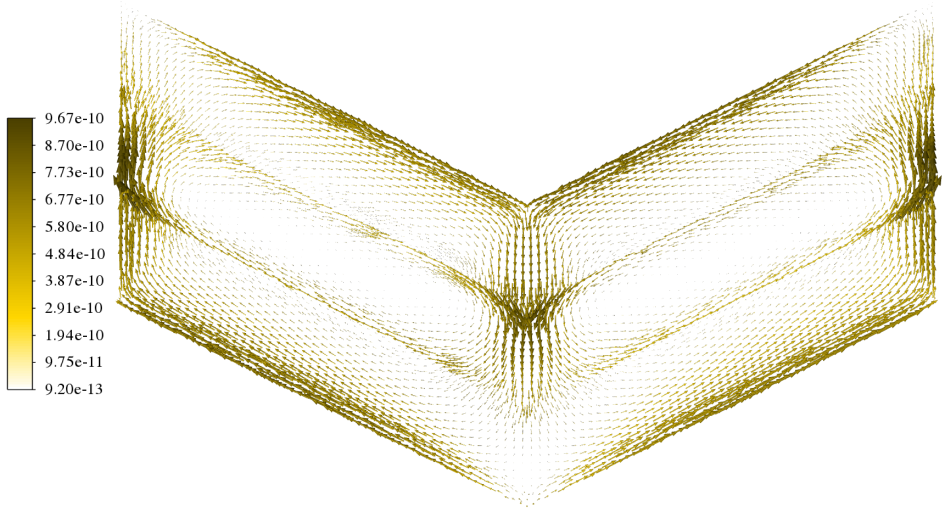


Fig. 15. Velocity vector field **V** [m/s] in plane A at $K_p = 5$

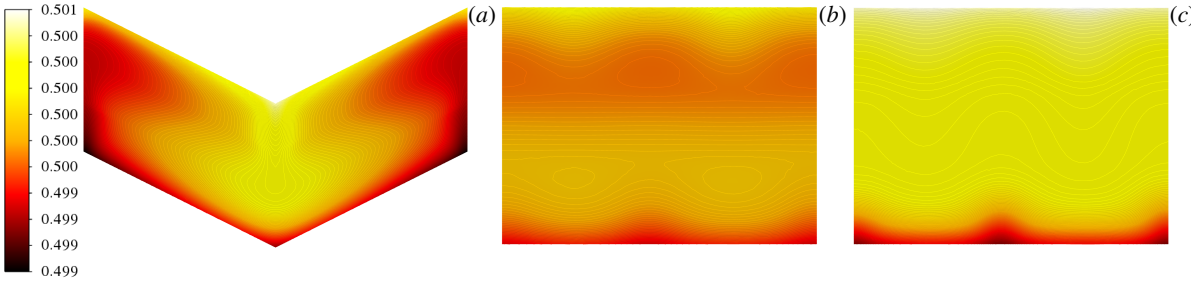


Fig. 16. Impurity concentration fields at $K_p = 5$ in planes A (*a*), D (*b*), and C (*c*)

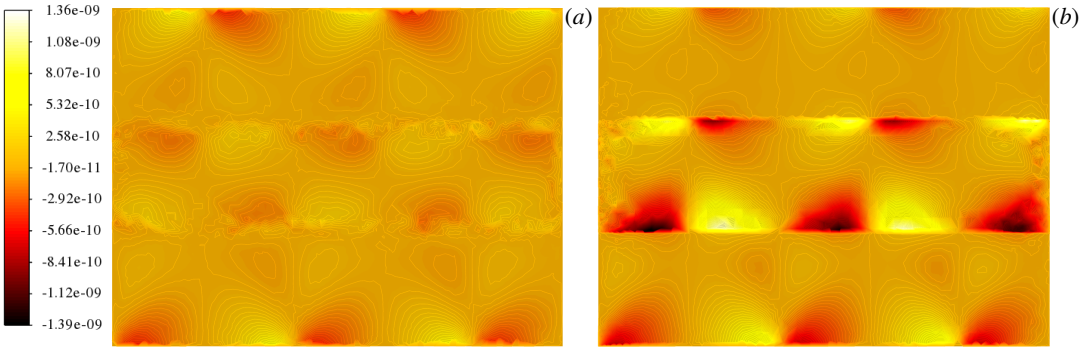


Fig. 17. Fields of the velocity component V_z [m/s] at $K_p = 10$ in planes D (*a*) and C (*b*)

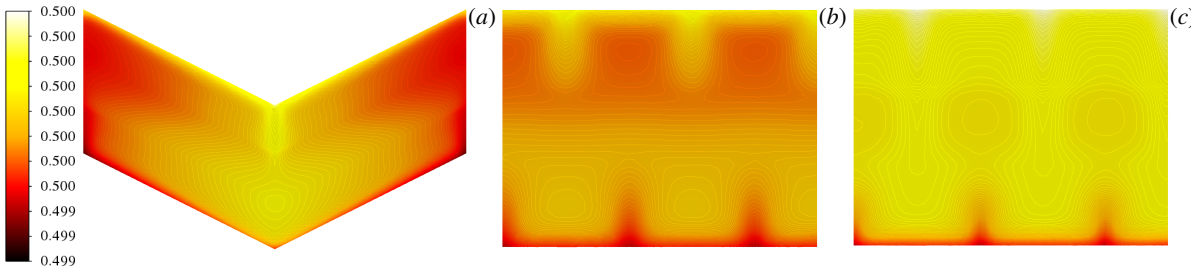


Fig. 18. Impurity concentration fields at $K_p = 10$ in planes A (*a*), D (*b*), and C (*c*)

7. Conclusion

As a result of nonlinear three-dimensional modeling, the following has been established:
– when the permeability of the inner layer is significantly higher than that of the outer layers, the flow is localized in the inner layer;
– when the permeabilities of the outer and inner layers are sufficiently close, the main flow shifts to the outer layers and concentrates near the fold walls, even though the inner layer remains more permeable than the outer ones;
– as the supercriticality increases, a longitudinal-roll component begins to appear in the initially plane-parallel flow (within each fold limb), and the flow becomes spiral;
– with a further increase in supercriticality, the longitudinal-roll component starts to dominate the flow, and the number of longitudinal rolls within a fold limb increases (for the longitudinal rolls, their wave number becomes larger);
– the appearance of the longitudinal component of the convective flow significantly affects the distribution of impurity concentration throughout the fold;
– in a synclinal geological fold, flow structures qualitatively analogous to those characteristic of an anticlinal fold are observed, except for the impurity concentration distribution over the fold.

The work was carried out as part of a major scientific project funded by the Ministry of Science and Higher Education of the Russian Federation (Agreement No. 075-15-2024-535 dated April 23, 2024).

References

1. *Billings M.P.* Structural geology. Prentice-Hall Inc., 1972. 606 p.

2. *Mikhaylov A.E.* Strukturnaya geologiya i geologicheskoye kartirovaniye. Moscow: Nedra, 1984. 464 p.

3. *Szulczewski M.L.*, *Hesse M.A.*, *Juanes R.* Carbon dioxide dissolution in structural and stratigraphic traps. Journal of Fluid Mechanics. 2013. Vol. 736. P. 287–315. DOI: 10.1017/jfm.2013.511

4. *Simmons C.T.*, *Bauer-Gottwein P.*, *Graf T.*, *et al.* Variable density groundwater flow: from modelling to applications. Groundwater Modelling in Arid and Semi-Arid Areas / ed. by H. Wheater, S. Mathias, X. Li. Cambridge University Press, 2010. P. 87–118. DOI: 10.1017/CBO9780511760280.008

5. *Baghooee H.*, *Montel F.*, *Galliero G.*, *Yan W.*, *Shapiro A.* A new approach to thermal segregation in petroleum reservoirs: Algorithm and case studies. Journal of Petroleum Science and Engineering. 2021. Vol. 201. 108367. DOI: 10.1016/j.petrol.2021.108367

6. *Parameswari K.*, *Mudgal B.V.* Assessment of contaminant migration in an unconfined aquifer around an open dumping yard: Perungudi a case study. Environmental Earth Sciences. 2015. Vol. 74, no. 7. P. 6111–6122. DOI: 10.1007/s12665-015-4634-x

7. *Hewitt D.R.*, *Neufeld J.A.*, *Lister J.R.* High Rayleigh number convection in a porous medium containing a thin low-permeability layer. Journal of Fluid Mechanics. 2014. Vol. 756. P. 844–869. DOI: 10.1017/jfm.2014.478

8. *Zech A.*, *Zehner B.*, *Kolditz O.*, *Attinger S.* Impact of heterogeneous permeability distribution on the groundwater flow systems of a small sedimentary basin. Journal of Hydrology. 2016. Vol. 532. P. 90–101. DOI: 10.1016/j.jhydrol.2015.11.030

9. *Salibindla A.K.R.*, *Subedi R.*, *Shen V.C.*, *Masuk A.U.M.*, *Ni R.* Dissolution-driven convection in a heterogeneous porous medium. Journal of Fluid Mechanics. 2018. Vol. 857. P. 61–79. DOI: 10.1017/jfm.2018.732

10. *Soboleva E.B.* Density-driven convection in an inhomogeneous geothermal reservoir. International Journal of Heat and Mass Transfer. 2018. Vol. 127. P. 784–798. DOI: 10.1016/j.ijheatmasstransfer.2018.08.019

11. *Zubova N.A.*, *Lyubimova T.P.* Convection of ternary mixture in anisotropic porous medium. 29th Russian Conference on Mathematical Modelling in Natural Sciences. Vol. 2371. 2021. 050013. DOI: 10.1063/5.0059568

12. *Zubova N.A.*, *Lyubimova T.P.* Nonlinear convection regimes of a ternary mixture in a two-layer porous medium. Computational Continuum Mechanics. 2021. Vol. 14, no. 1. P. 110–121. DOI: 10.7242/1999-6691/2021.14.1.10

13. *Barbier E.* Geothermal energy technology and current status: an overview. Renewable and Sustainable Energy Reviews. 2002. Vol. 6. P. 3–65. DOI: 10.1016/S1364-0321(02)00002-3

14. *Kocberber S.*, *Collins R.E.* Impact of Reservoir Heterogeneity on Initial Distributions of Hydrocarbons. SPE Annual Technical Conference and Exhibition. 1990. P. 175–201. DOI: 10.2118/20547-MS

15. *Schmitt R.W.* Double Diffusion in Oceanography. Annual Review of Fluid Mechanics. 1994. Vol. 26. P. 255–285. DOI: 10.1146/annurev.fl.26.010194.001351

16. *Pedersen K.S.*, *Hjermstad H.P.* Modeling of Compositional Variation with Depth for Five North Sea Reservoirs. SPE Annual Technical Conference and Exhibition. 2015. DOI: 110.2118/175085-ms

17. *Collell J.*, *Galliero G.*, *Vermorel R.*, *Ungerer P.*, *Yiannourakou M.*, *Montel F.*, *Pujol M.* Transport of Multicomponent Hydrocarbon Mixtures in Shale Organic Matter by Molecular Simulations. The Journal of Physical Chemistry C. 2015. Vol. 119, no. 39. P. 22587–22595. DOI: 10.1021/acs.jpcc.5b07242

18. *Lyubimova T.P.*, *Muratov I.D.*, *Shubenkov I.S.* Onset and nonlinear regimes of convection in an inclined porous layer subject to a vertical temperature gradient. Physics of Fluids. 2022. Vol. 34. 094114. DOI: 10.1063/5.0104575

19. *Shubenkov I.*, *Lyubimova T.*, *Sadilov E.* Three-Dimensional Convection in an Inclined Porous Layer Subjected to a Vertical Temperature Gradient. Fluid Dynamics & Materials Processing. 2024. Vol. 20, no. 9. P. 1957–1970. DOI: 10.32604/fdmp.2024.050167

20. *Lyubimova T.*, *Shubenkov I.*, *Ozhgibesova N.* Soret-Induced Convection in a Layered Porous Medium Simulating an Anticlinal Geological Fold Under the Action of a Geothermal Temperature Gradient. Heat Transfer. 2025. Vol. 54. P. 2251–2264. DOI: 10.1002/htj.23289

21. *Platten J.K.*, *Costeseque P.* The Soret Coefficient in Porous Media. Journal of Porous Media. 2004. Vol. 7, no. 4. P. 317–330. DOI: 10.1615/JPorMedia.v7.i4.60

22. *Yasnou V.*, *Mialdun A.*, *Melnikov D.*, *Shevtsova V.* Role of a layer of porous medium in the thermodiffusion dynamics of a liquid mixture. International Journal of Heat and Mass Transfer. 2019. Vol. 143. 118480. DOI: 10.1016/j.ijheatmasstransfer.2019.118480

23. *Alkhasov A.B.* Vozobnovlyayemyye istochniki energii. Moscow: Fizmatlit, 2012. 256 p.

24. *Forster S.*, *Bobertz B.*, *Bohling B.* Permeability of Sands in the Coastal Areas of the Southern Baltic Sea: Mapping a Grain-size Related Sediment Property. Aquatic Geochemistry. 2003. Vol. 9. P. 171–190. DOI: 10.1023/B:AQUA.0000022953.52275.8b

25. *Iscan A.G.*, *Kok M.V.* Porosity and Permeability Determinations in Sandstone and Limestone Rocks Using Thin Section Analysis Approach. Energy Sources, Part A. 2009. Vol. 31. P. 568–575. DOI: 10.1080/15567030802463984

26. Spravochnik (kadastr) fizicheskikh svoystv gornykh porod / ed. by N.V. Melnikov, V.V. Rzhevsky, M.M. Protodyakonov. Moscow: Nedra, 1975. 279 p.

27. *Dobrynin M.V.*, *Wendelstein B.Y.*, *Kozhevnikov D.A.* Petrofizika (fizika gornykh porod). Moscow: Federal State Budgetary Institution Oil, Gas Publishing House of the Russian State University of Oil, Gas named I.M. Gubkin, 2004. 368 p.

28. *Lobov N.I.*, *Lyubimov D.V.*, *Lyubimova T.P.* Resheniye zadach na EVM. Perm: Perm University, 2007. 82 p.

Authors' Details:

Ivan Sergeevich Shubenkov (corr.), Junior Researcher, Institute of Continuous Media Mechanics UB RAS (ICMM UB RAS), 1 Akademika Koroleva St., Perm, 614018, Russian Federation; e-mail: ShubenkovIS@yandex.ru; ORCID: 0000-0001-9682-9531

Tatiana Petrovna Lyubimova, Doctor of Physical and Mathematical Sciences, Professor, Head of Laboratory, ICMM UB RAS; e-mail: lyubimovat@mail.ru; ORCID: 0000-0002-8212-2890